



Two superconducting states with broken time-reversal symmetry in $FeSe_{1-x}S_x$

Kohei Matsuura^{a,1}, Masaki Roppongi^a, Mingwei Qiu^a, Qi Sheng^b, Yipeng Cai^{Cd}, Kohtaro Yamakawa^b, Zurab Guguchia^b, Ryan P. Day^{cd}, Kenji M. Kojima^{ce} 📵, Andrea Damascelli^{cd} 📵, Yuichi Sugimura 📵, Mikihiko Saito 📵, Takaaki Takenaka 📵, Kota Ishihara 📵, Yuta Mizukami^{a,2}, Kenichiro Hashimoto^a, Yilun Gu^f, Shengli Guo^f, Licheng Fu^f, Zheneng Zhang^f, Fanlong Ning^f, Guoqiang Zhao^{ghi}, Guangyang Dai^{ghi}, Changqing Jin^{gh,i}, James W. Beareⁱ, Graeme M. Luke^{e,i}, Yasutomo J. Uemura^{b,3}, and Takasada Shibauchi^{a,3}

Edited by Andrey Chubukov, University of Minnesota, Minneapolis, MN 55455; received May 13, 2022; accepted April 12, 2023, by Editorial Board Member Zachary Fisk

Iron-chalcogenide superconductors $FeSe_{1-x}S_x$ possess unique electronic properties such as nonmagnetic nematic order and its quantum critical point. The nature of superconductivity with such nematicity is important for understanding the mechanism of unconventional superconductivity. A recent theory suggested the possible emergence of a fundamentally new class of superconductivity with the so-called Bogoliubov Fermi surfaces (BFSs) in this system. However, such an ultranodal pair state requires broken time-reversal symmetry (TRS) in the superconducting state, which has not been observed experimentally. Here, we report muon spin relaxation (μ SR) measurements in $\text{FeSe}_{1-x}S_x$ superconductors for $0 \le x \le 0.22$ covering both orthorhombic (nematic) and tetragonal phases. We find that the zero-field muon relaxation rate is enhanced below the superconducting transition temperature T_c for all compositions, indicating that the superconducting state breaks TRS both in the nematic and tetragonal phases. Moreover, the transverse-field µSR measurements reveal that the superfluid density shows an unexpected and substantial reduction in the tetragonal phase (x > 0.17). This implies that a significant fraction of electrons remain unpaired in the zero-temperature limit, which cannot be explained by the known unconventional superconducting states with point or line nodes. The TRS breaking and the suppressed superfluid density in the tetragonal phase, together with the reported enhanced zeroenergy excitations, are consistent with the ultranodal pair state with BFSs. The present results reveal two different superconducting states with broken TRS separated by the nematic critical point in $FeSe_{1-x}S_x$, which calls for the theory of microscopic origins that account for the relation between nematicity and superconductivity.

iron-based superconductors | superconducting gap | muon spin relaxation | unconventional superconductivity | Bogoliubov Fermi surface

Recent studies of FeSe_{1-x}S_x using high-quality single crystals up to $x \sim 0.25$ have shown that electronic nematic order sets in at the structural transition temperature T_s , which can be completely suppressed by S substitution without inducing any magnetic ordering under ambient pressure (1, 2). The phase diagram of $FeSe_{1-x}S_x$ exhibits a nematic quantum critical point at $x \approx 0.17$ (3, 4), near which anomalous non-Fermi liquid transport properties have been reported (5, 6). The superconducting gap structure of $FeSe_{1-x}S_x$ inside the nematic (orthorhombic) phase is very anisotropic, and it has been discussed that $\Delta(\mathbf{k})$ exhibits accidental line nodes or deep minima (7–12), indicating the unconventional nature of its superconductivity. In the nematic phase with C_2 symmetry, the superconducting gap has twofold rotational symmetry, which can be described by the sum of two contributions Δ_s and Δ_d having s-wave and d-wave symmetries, respectively (13, 14). We should also consider the effect of nematic domains whose orientations are orthogonal to each other, and in neighboring domains, one of the s- and d-wave contributions has opposite signs, such as $\Delta_s \pm \Delta_d$ (13). Scanning tunneling microscopy (STM) and angle-resolved photoemission spectroscopy (ARPES) studies on FeSe have shown that the nematic twin boundary affects the low-energy excitation spectrum, opening a gap near the boundary (8, 11). It has been suggested that across the twin boundary, $\Delta_s + \Delta_d$ may be transformed into $\Delta_s - \Delta_d$ through a time-reversal symmetry breaking (TRSB) state $\Delta_s + e^{i\theta} \Delta_d$ with $0 < \theta < \pi$, which is consistent with the gap opening near the boundary. However, direct evidence of TRSB has not been reported in superconducting FeSe.

In the tetragonal phase of $FeSe_{1-x}S_x$ (x > 0.17), the nematic order disappears, and thus, no twin boundary is observed in the STM measurements (15). It has been

Significance

When metal becomes superconducting, the Fermi surface becomes unstable, and a superconducting gap forms. In unconventional superconductors, the gap varies in momentum space and can become zero at points or lines on the original Fermi surface. More exotic superconducting states with time-reversal symmetry breaking (TRSB) have been theoretically proposed, but such states are rarely found. Our muon experiments on iron chalcogenide superconductors $FeSe_{1-x}S_x$ in the orthorhombic and tetragonal phases provide evidence for TRSB below the transition temperatures. Moreover, the TRSB superconducting state in the tetragonal phase has a unique feature that not all electrons become superconducting. Our results reveal that this system exhibits two distinct superconducting states both with TRSB, which provides research directions for exotic superconductivity.

Copyright © 2023 the Author(s), Published by PNAS. This article is distributed under Creative Commons Attribution-NonCommercial-NoDerivatives License 4.0 (CC BY-NC-ND).

¹Present address: Department of Applied Physics, University of Tokyo, Bunkyo-ku, Tokyo 113-8656, Japan.

²Present address: Department of Physics, Tohoku University, Aoba-ku, Sendai, Miyagi 980-8578, Japan.

³To whom correspondence may be addressed. Email: yu2@columbia.edu or shibauchi@k.u-tokyo.ac.jp.

This article contains supporting information online at http://www.pnas.org/lookup/suppl/doi:10.1073/pnas. 2208276120/-/DCSupplemental.

Published May 15, 2023.

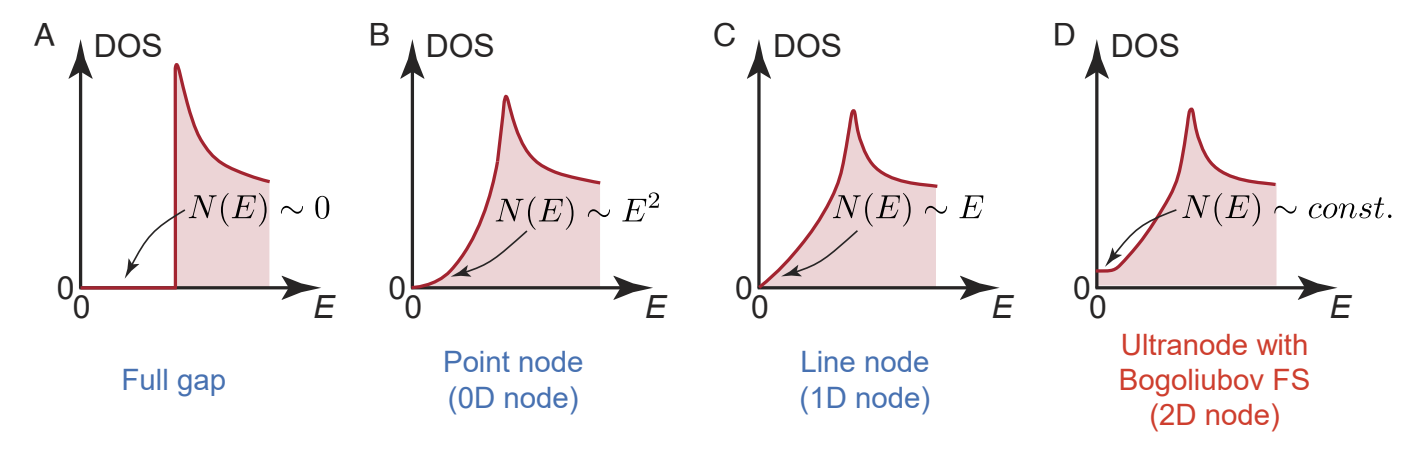


Fig. 1. Classification of low-energy quasiparticle excitations with different nodal structures of the superconducting gap. (A) Systematic energy dependence of quasiparticle density of states N(E) for fully gapped superconductors with no nodes. (B) For superconductors with point nodes, the Fermi surfaces in the normal state are gapped except for the nodal points and N(E) follows E^2 dependence at low energies. (C) When the superconducting gap has lines of nodes, N(E) obeys E-linear dependence at low energies in the absence of a magnetic field. (D) A new class of superconducting gap structure exhibits 2D surfaces of nodes in the superconducting state. In this case, TRS has to be broken, and extended zero-energy excitations give finite N(0), similar to metallic states with Fermi surfaces.

reported that although the electronic structure evolves smoothly across the critical concentration (15, 16), the superconducting properties change abruptly (15, 17, 18). In the tetragonal phase, the STM conductance spectra in the superconducting state have found a substantial zero-bias value, and the specific heat and thermal conductivity show large residuals at low temperatures.

Recent theoretical studies have suggested that $FeSe_{1-x}S_x$ may have an ultranodal superconducting state with Bogoliubov Fermi surfaces (BFSs), which can account for these unusual properties reported in the tetragonal phase. In conventional s-wave superconductors, the gap is almost isotropic in momentum space, and the quasiparticle density of state N(E) is essentially absent at low energies (Fig. 1A). In unconventional superconducting states, the superconducting gap $\Delta(\mathbf{k})$ on the normal-state Fermi surfaces may have points or lines of zeros (nodes). Consequently, the low-energy quasiparticle excitations are governed by the nodal structure, as summarized in Fig. 1 B and C. In contrast, the novel ultranodal superconducting state has extended two-dimensional surfaces of nodes ($\Delta(\mathbf{k}) = 0$). These BFSs lead to extended zero energy states at zero field like a normal metal (Fig. 1D). It has been shown theoretically by Agterberg et al. (19, 20) that such an exotic pairing state with BFSs can be energetically stable under certain conditions, if the system breaks TRS. A recent theoretical study considers a multiband system with intraband and interband interactions with broken TRS and suggests an ultranodal pair state with BFSs, which may apply to FeSebased superconductors (21, 22). It is then extremely important to clarify whether TRS is broken or not in the $FeSe_{1-x}S_x$ experimentally.

Results

TRSB in the superconducting state can be studied by the zerofield muon spin relaxation (μ SR) technique, which is a sensitive probe of the internal magnetic field inside the sample (23). When TRS is broken in the superconducting state, a small magnetic field can be induced near defects or TRSB domain boundaries (24), which can be detected by the change in the relaxation rate of μSR asymmetry. As shown in Fig. 2 A-C, we have measured zerofield μ SR spectra at low temperatures for the collection of single crystals of FeSe (x = 0) in the nematic phase and FeSe_{1-x}S_x

(x = 0.20 and 0.22) in the tetragonal phase. The comparisons of relaxation curves in the normal state above T_c (red symbols) and in the superconducting state below T_c (blue symbols) reveal a faster relaxation in the superconducting state for all samples. The relaxation rate Λ of the samples can be extracted through the fitting analysis considering background contributions (SI *Appendix*), and the obtained temperature dependence of Λ is shown in Fig. 2 D-F. The small and almost temperatureindependent relaxation in the normal state is likely due to randomly oriented nuclear magnetic moments whose fluctuation speed is slower than the μSR time scale. For all the samples we measured, the relaxation rate increases below T_c , and the increase in Λ is observed in both non-spin-rotated (NSR) and spin-rotated (SR) configuration modes (Fig. 2E). These results indicate that a finite magnetic field develops in the sample in the superconducting state. Moreover, for the samples tested under longitudinal magnetic fields of 200–2,000 G (x = 0 and 0.22), we find that the relaxation rate shows no enhancement below T_c (Fig. 2 D and F), implying that the internal field below T_c observed in the zero-field μ SR measurements is not fluctuating but static on the microsecond timescale. The increase of the relaxation rate is similar in magnitude both in the nematic and tetragonal phases, and the internal magnetic field at the lowest temperatures can be estimated as $B_{int} \sim 0.09$, 0.12, and 0.07 G for x = 0, 0.20, and 0.22, respectively (Fig. 2 D–F). These values are significantly larger than the inevitable residual field (<5 mG) in our shielded experimental setup. These results strongly indicate that TRS is broken in both nematic and tetragonal phases of superconducting $FeSe_{1-x}S_x$.

In addition to the zero-field measurements, we have also performed the transverse-field μ SR measurements under external fields of 330 G. From the relaxation rate analysis in the superconducting state (SI Appendix), we can extract the temperature dependence of the superfluid density, which is proportional to $\lambda^{-2} \propto n_s/m^*$, where λ is the in-plane magnetic penetration depth and m^* is the effective mass of quasiparticles. This gives information on the superconducting electron density n_s , which can be compared with the total electron density n. The temperature dependence of λ^{-2} for x = 0 and 0.10 in the nematic phase and for x = 0.20 and 0.22 in the tetragonal phase is shown in Fig. 3A. The data for all samples deviate from the

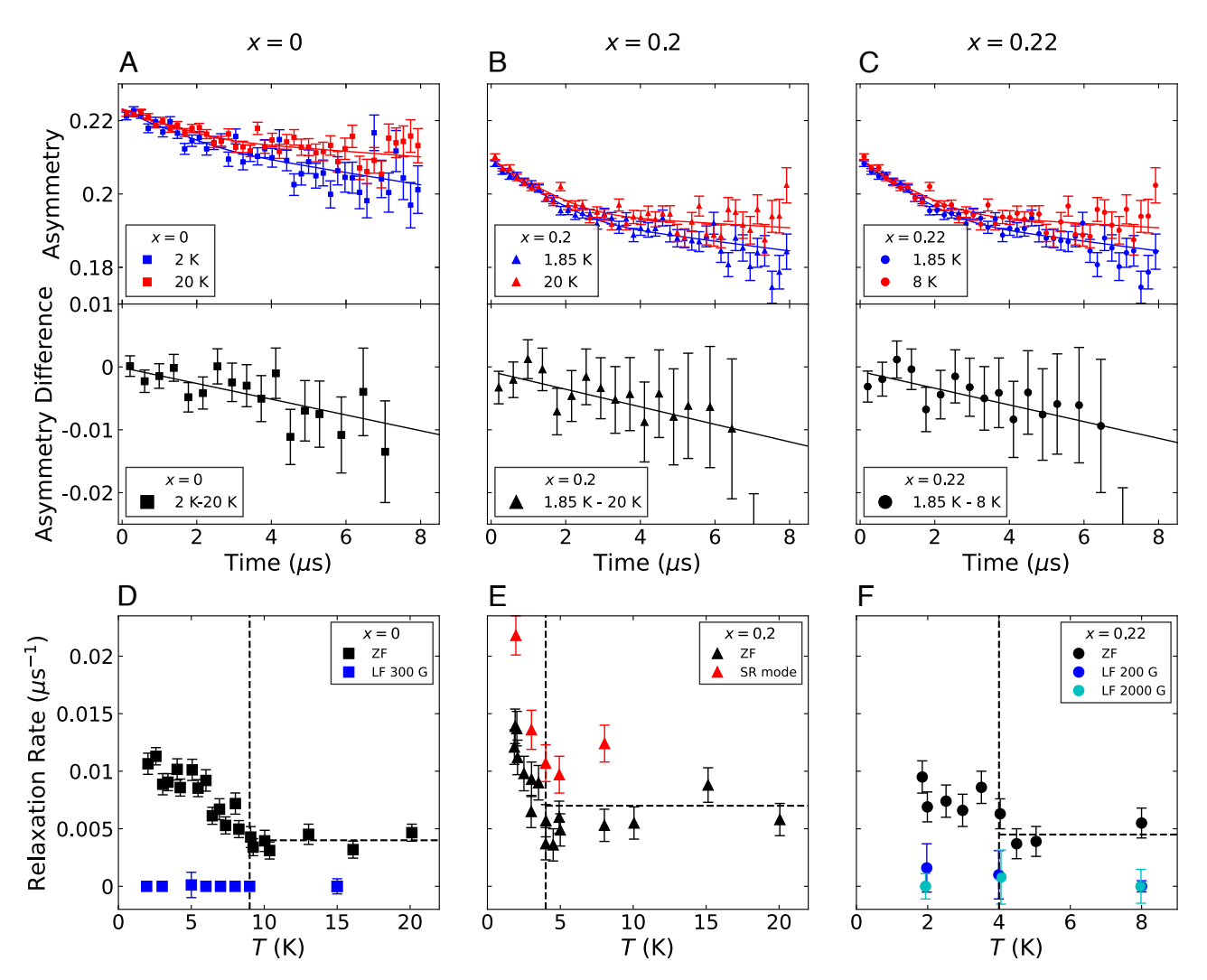
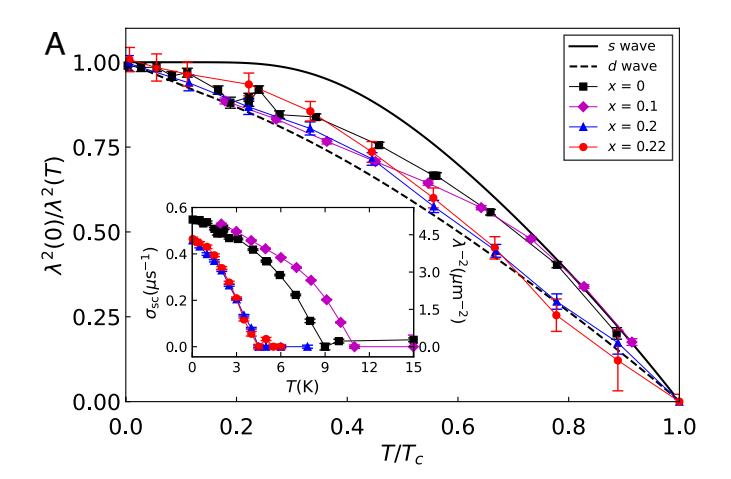


Fig. 2. Evidence for TRS breaking superconductivity from zero-field μ SR. (A–C) Time evolution of μ SR asymmetry in the NSR mode for FeSe (A) in the nematic phase and for FeSe $_{1-x}$ S $_x$ with x=0.20 (B) and 0.22 (C) in the tetragonal phase. *Upper panels* show the data compared at two temperatures above T_C in the normal state (red) and below T_C in the superconducting state (blue). Curves are fits to the relaxation curve described in *SI Appendix*, Eq. **S1**. *Lower panels* show the difference of the data (symbols) between the two temperatures. The lines are the guides to the eyes. (D–F) Temperature dependence of the relaxation rate A0 extracted from the fitting analysis for FeSe (D1) in the nematic phase and for FeSe $_{1-x}$ S $_x$ with X0.20 (F1) and 0.22 (F1) in the tetragonal phase. For all samples, we use the NSR mode (black), but for X0.20, the SR mode is also used (red). The muon polarization is along the C0 axis (C0) and 0.22 (C1) in the NSR (SR) mode. In both modes, similar temperature dependence of C1 is observed. For comparison, the results of the relaxation rate in longitudinal-field C1 in the NSR (SR) measurements up to 2,000 G (blue) are shown for C2 (C3) and 0.22 (C5). Vertical dashed lines mark the transition temperature C2. Horizontal dashed lines are guides to the eyes.

conventional s-wave curve, consistent with the anisotropic gap in this system. We also note that the $\lambda^{-2}(T)$ data for FeSe (x=0) are in good agreement with the previous μ SR measurements for a 500-G c-axis field (25) (SI Appendix, Fig. S3). The absolute values of λ^{-2} in the zero-temperature limit become smaller in the tetragonal phase compared with those in the nematic phase (Fig. 3 A, Inset). Notably, this is opposite to the increasing trend of Fermi surface volumes as a function of x in FeSe_{1-x}S_x reported from the quantum oscillation measurements (16).

More quantitatively, in Fig. 4C, we compare the x-dependence of $\lambda^{-2}(T\to 0)$ measured by μSR and that estimated from the Fermi surface structures based on quantum oscillations measurements (16) (SI Appendix). In FeSe (x = 0), the $\lambda^{-2}(T\to 0)$ value is quantitatively consistent with the estimate from all measured orbits in quantum oscillations, indicating that all the carriers in the normal state are condensed into the superconducting pairing state. The comparison between measured and estimated λ^{-2} in FeSe_{1-x}S_x (Fig. 4C) demonstrates

that the superfluid density in the tetragonal phase is substantially suppressed from that expected from the normal-state electronic structure. Together with the reported phase diagram (Fig. 4A) and the evolution of low-energy excitations with S composition x (Fig. 4B), we can summarize the unusual transformation of the superconducting state from the SC1 phase to SC2 phase, driven by the disappearance of the nematic order in $FeSe_{1-x}S_x$, as follows. i) The superconducting transition temperature T_c shows an abrupt change between SC1 in the nematic phase and SC2 in the tetragonal phase (18). ii) The zero-bias tunneling conductance (15) and electronic specific heat (17, 18) at low temperatures are both largely enhanced in the SC2 phase, indicating the presence of low-lying quasiparticle excitations in the tetragonal phase. iii) The superfluid density shows a sizable suppression in the SC2 phase from that expected from the normal-state electronic structure. iv) TRS is broken in both SC1 and SC2 phases. These results indicate that $FeSe_{1-x}S_x$ exhibits two different TRSB superconducting states SC1 and SC2, which are separated by the end point of the nematic order.



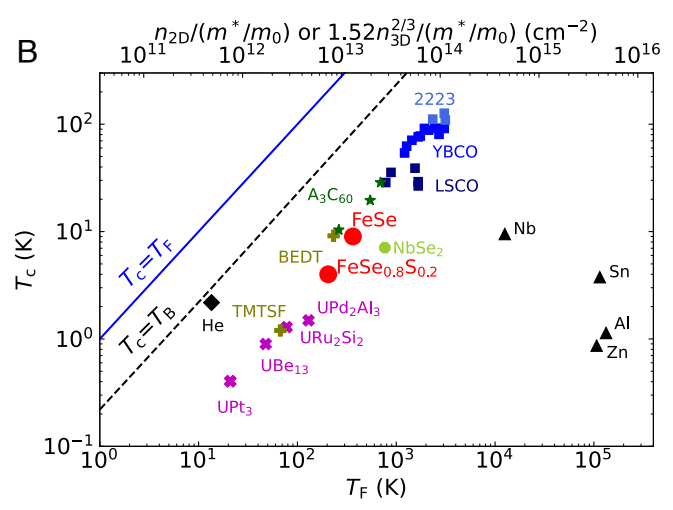


Fig. 3. Superfluid density from transverse-field μ SR. (A) Normalized superfluid density $\lambda^2(0)/\lambda^2(T)$ as a function of reduced temperature T/T_c for $FeSe_{1-x}S_X$ with x = 0, 0.10, 0.20, and 0.22. The solid (dashed) curve is the theoretical temperature dependence of superfluid density in the conventional fully gapped s-wave (line-nodal d-wave) superconductors. The Inset shows the temperature dependence of relaxation rate σ_{SC} in the superconducting state (*Left* axis) and superfluid density $\lambda^{-2}(T)$ without normalization (*Right* axis). (B) Uemura plot, where T_{C} is plotted against the effective superfluid density (*Upper* axis). The effective superfluid density is given by $n_{\rm 2D}/(m^*/m_0)$ and 1.52 $n_{\rm 3D}$ for the 2D and 3D systems, respectively, where $n_{\rm 2D}$ is the carrier concentration in the superconducting plane of the 2D system, $n_{\rm 3D}$ is the carrier concentration of the 3D system, and \emph{m}_{0} is the mass of the free electron. The Fermi temperature T_F (Lower axis) is proportional to the effective carrier density n_{2D} , with the relation $T_{\rm F}=h^2\pi n_{2D}/(k_Bm^*)$. In this study, we assumed that FeSe_{1-x}S_x is in the limit of a highly anisotropic superconductor and used a two-dimensional expression. The black dashed line is the Bose-Einstein condensation temperature of an ideal three-dimensional boson gas. The solid blue line shows the line where $T_c = T_F$.

The suppressed superfluid density in the tetragonal phase implies that not all electrons are condensed in the superconducting ground state, which is quite anomalous. The presence of unpaired electrons in the zero-temperature limit is not expected even in nodal superconductors but consistent with the presence of zero-energy excitations reported by the STM and specific heat measurements. These results in the SC2 phase are consistent with an ultranodal pair state with emergent BFSs suggested theoretically.

Discussion

Here, we emphasize that the crystals used in this study are grown by the chemical vapor transport technique (3, 26),

which is known as a method to obtain high-quality FeSe-based samples (1). The observation of quantum oscillations in a wide range indicates that the crystals are clean, and the STM results show that S atoms are distributed quite uniformly (15, 16). It is therefore highly unlikely that the low-lying excitations in SC2 originate from impurities or chemical inhomogeneities. This is reinforced by the STM measurements in the tetragonal phase, which have shown that the presence of zero-bias conductance is a robust feature insensitive to the positions (15). The fact that the onsets of these extraordinary excitations and the suppressions of T_c and λ^{-2} match the fate of the nematic order strongly suggests that the emergence of an ultranodal state is an intrinsic property triggered by the electronic change associated with the nematicity in this system.

One may also consider the effect of multigap and the possibility of gapless Fermi surface in some bands, which could lead to the unpaired electrons. However, it has been widely discussed that the interband interactions are generally important for iron-based superconductors, and thus, there must be nonnegligible coupling between different bands. In such a case, it is natural to consider that all the bands have superconducting ground states even if they have different gap magnitudes. In principle, some of the bands may have very small gaps, but the temperature dependence of the superfluid density down to very low temperatures (Fig. 3A) does not show any signatures of such an extremely small gap. Thus, we conclude that the multigap effect is unlikely the origin of the unpaired electrons.

We should note that the theoretical model of ultranodal states for $FeSe_{1-x}S_x$ does not provide microscopic origins at present (21). Moreover, it is not clear how the BFSs can relate to nematicity. Thus, a complete understanding of the observed behaviors requires further studies. However, in recent theoretical calculations of the diamagnetic current response, it has been shown that there is a limited range of degree of TRSB to have stable BFSs, in which the superfluid density becomes less than half of the original value (22). This appears to be in good correspondence with the case for SC2 in the tetragonal phase of FeSe_{1-x}S_x.

The observed TRSB in the nematic phase of FeSe, in which no evidence of BFSs is found, also poses an intriguing question about the structure of the phase of the order parameter in the presence of the nematic twin boundary. As mentioned above, near the nematic twin boundary, we expect a large change in the phase θ in the complex order parameter $\Delta_s + e^{i\theta} \Delta_d$. If the TRS is preserved deep inside the bulk, we expect $\theta = 0$ or π away from the boundaries. Our zero-field μ SR results show a similar change of relaxation rate below T_c in FeSe and tetragonal FeSe_{1-x}S_x with and without nematic twin boundaries, which imply that TRS is broken inside the bulk even for FeSe. In such a nematic TRSB superconducting state, θ is shifted from 0 or π in the bulk, but still, θ is different in the neighboring domains, and the phase can change near twin boundaries. This suggests that the degree of TRSB depends on the position near twin boundaries, which can explain the STM and ARPES results. Indeed, the original theory considering the orthorhombic domains by Sigrist et al. (13) has shown that the state with broken TRS only near twin boundaries exists in a limited temperature region above the bulk TRSB state. In FeSe, the superconducting gap structure is very anisotropic and twofold symmetric around the hole and electron bands (10, 11), which suggests that Δ_s and Δ_d have similar magnitudes. In such a case, it is plausible that the TRSB sets in very close to T_c , which seems consistent with the observed enhancement of the relaxation rate just below T_c .

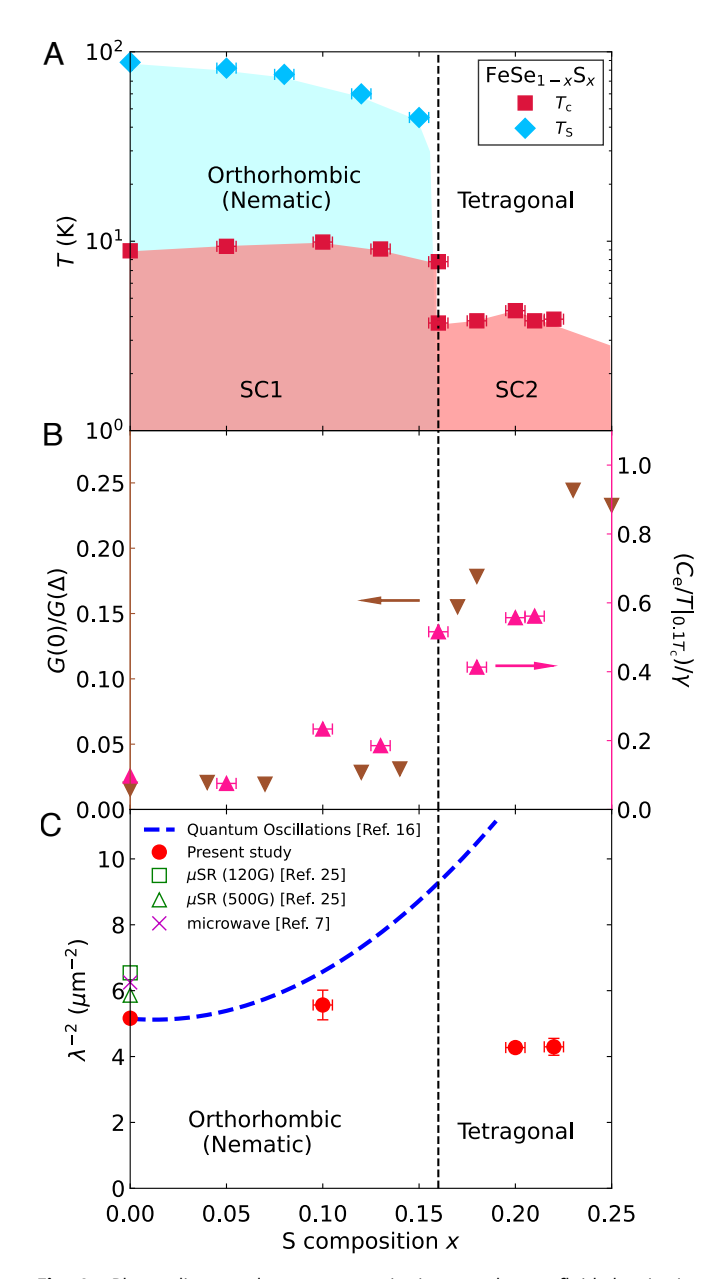


Fig. 4. Phase diagram, low-energy excitations, and superfluid density in $FeSe_{1-x}S_x$. (A) Thermodynamically determined phase diagram of $FeSe_{1-x}S_x$. The high-temperature tetragonal to low-temperature orthorhombic (nematic) transition temperature T_S and superconducting transition temperature T_{c} are determined by specific heat measurements using vapor-grown single crystals (18). (B) Zero-bias tunneling conductance G(0) normalized by the conductance at the gap edge $G(\Delta)$ measured by STM (15) and the low-temperature electronic specific heat divided by temperature C_e/T at $T=0.1T_{\rm C}$ normalized by the Sommerfeld constant γ (18), plotted against S composition x in FeSe_{1-x}S_x single crystals. (C) Evolution of superfluid density in the zero-temperature limit (red squares) with x, compared with the estimated λ^{-2} from the normal-state Fermi surface structure (dashed line) based on the quantum oscillations measurements (16) (SI Appendix). The previously reported values of λ^{-2} in FeSe (x=0) from μ SR measurements for 120 G (cross) and 500 G (square) (25) and from microwave surface impedance measurements in the Meissner state (triangle) (7) are also shown for comparison (*SI Appendix*, Fig. S3). The vertical error bars are estimated from various fittings of $\lambda^{-2}(T)$.

In addition to the TRSB and gap node topology, our present results for the superfluid density provide insights into phenomenologies of unconventional superconductors. Figure 3B shows correlations between T_c and the effective Fermi tem-

perature $T_F = E_F/k_B$ derived from the effective superfluid density n_s/m^* (27, 28). The points from FeSe_{1-x}S_x lie close to the nearly linear trend between T_c and T_F reported in hole-doped and electron-doped cuprates, organic, and heavy-fermion superconductors (27, 28), which is a hallmark of strongly correlated superconductivity. This may suggest that the sudden decrease in T_c above the nematic end point is closely related to the reduction in the superfluid density due to the emergence of BFSs in the tetragonal phase (Fig. 4 A and C). The doping evolution of FeSe_{1-x}S_x resembles the behaviors of overdoped cuprates, in the departure of superfluid density from the normal-state carrier density (28), existence of nematic quantum critical point (29), and orthorhombic to tetragonal transition. This analogy encourages high-precision experimental searches for TRSB in overdoped cuprates.

Our μ SR measurements reveal two different TRSB superconducting states in the phase diagram of FeSe_{1-x}S_x. The suppression of nematicity leads to the reduction in T_c as well as the suppressed superfluid density, which indicates that the superconductivity in the tetragonal phase is very exotic, having broken TRS and unpaired electrons. The results are consistent with the ultranodal state with BFSs proposed theoretically, but details of the BFSs including the size and the location in the momentum space require further studies. Together with the recent reports of Bose–Einstein condensation-like superconductivity in FeSe_{1-x}S_x (18, 30), our findings may open up a wide field of studies on the extended zero-energy excitations in fermionic bound states.

Materials and Methods

Single Crystals. Single crystals of FeSe_{1-x}S_x (x = 0, 0.10, 0.20, and 0.22) used in this study were synthesized by the chemical vapor transport method (3, 26). For the μ SR measurements, a sample mass density of about 200 mg/cm² is required to stop the muon in the sample. For the pure FeSe samples, typical crystal dimensions are about $1 \times 1 \text{ mm}^2$ in the ab plane and several tens of μm in the c-axis direction and weigh about 1 to 5 mg. The sizes of the S-substituted samples are even smaller. Therefore, for each x, a large number of single-crystal samples (up to 100 pieces) were coaligned on a silver plate with Apiezon N grease (whose volume is around 10% of the sample mass) to cover an area of ~ 1 cm², so that the c axes were aligned perpendicular to the plate. For x = 0, 0.10, and 0.22, crystals were collected from a single batch each, but for x = 0.20, we used a few batches to extract enough crystals with a total mass of ~ 170 mg. Energy-dispersive X-ray spectroscopy was used to determine the compositions of S-substituted samples by averaging the x values obtained for several samples taken from the batches. For x = 0.22, we also measured the temperature dependence of resistivity on a crystal taken from the same batch, and it was confirmed that there was no anomaly due to structural phase transition and that the superconducting transition temperature was around 4 K. In addition, the c-axis lattice parameters determined by X-ray diffraction experiments are consistent with the previous reports (3, 26).

μSR Measurements Analysis. μSR measurements were performed at the Centre for Molecular and Materials Science at TRIUMF in Vancouver, Canada. We conducted zero-field μSR measurements above 2 K with the M20D beamline, while the measurements below 2 K were conducted on the M15 surface muon channel with a dilution refrigerator. Stray magnetic fields at the sample position at M20D were measured by fluxgate magnetometer and found to be ~ 2 , 1, and 5 mG along three orthogonal directions. Stray fields were reduced to less than 5 mG in all directions in the dilution refrigerator using the method of ref. 31. The μSR analysis was performed in the time domain using the program MUSRFIT (32). More detailed information for the procedure of data analysis is described in SI Appendix.

Data, Materials, and Software Availability. All study data are included in the article and/or *SI Appendix*.

ACKNOWLEDGMENTS. We thank D. F. Agterberg, P. M. R. Brydon, R. M. Fernandes, T. Hanaguri, P. J. Hirschfeld, K. Kuboki, Y. Matsuda, E.-G. Moon, C. Setty, and M. Sigrist for fruitful discussions. This work was supported by Grants-in-Aid for Scientific Research (Nos. JP22H00105, JP21H01793, JP19H00649, JP18H05227, and JP18KK0375), Grant-in-Aid for Scientific Research on innovative areas "Quantum Liquid Crystals" (No. JP19H05824) and Grant-in-Aid for Scientific Research for Transformative Research Areas (A) "Condensed Conjugation" (No. JP20H05869) from Japan Science and Technology. The work at Columbia and TRIUMF has been supported by the US NSF Grant Nos. DMR-2104661, DMR-1610633, and the DMREF Project No. DMR-1436095, the Reimei Project from the Japan Atomic Energy Agency, and a support from the Friends of Tokyo University Inc. G.Q.Z. has been supported in part by CAS Project for Young Scientists in Basic Research (2022YSBR-048). This research was undertaken thanks in part to funding from the Max Planck-UBC-

- . T. Shibauchi, T. Hanaguri, Y. Matsuda, Exotic superconducting states in FeSe-based materials. J. Phys. Soc. Jpn. 89, 102002 (2020).
- A. I. Coldea, Electronic nematic states tuned by isoelectronic substitution in bulk FeSe_{1-x}S_x. Front. Phys. 8, 594500 (2021).
- S. Hosoi et al., Nematic quantum critical point without magnetism in FeSe_{1-x}S_x superconductors. Proc. Natl. Acad. Sci. U.S.A. 113, 8139-8143 (2016).
- K. Ishida et al., Pure nematic quantum critical point accompanied by a superconducting dome. Proc. Natl. Acad. Sci. U.S.A. 119, e2110501119 (2022).
- S. Licciardello et al., Electrical resistivity across a nematic quantum critical point. Nature 567, 213–217 (2019)
- W. K. Huang et al., Non-Fermi liquid transport in the vicinity of the nematic quantum critical point of superconducting FeSe_{1-x}S_x. Phys. Rev. Res. 2, 033367 (2020).
 S. Kasabara et al., Field induced graphs and the property of FeSe in the PCC PEC graph of the PCC PEC graph
- S. Kasahara et al., Field-induced superconducting phase of FeSe in the BCS-BEC cross-over. Proc. Natl. Acad. Sci. U.S.A. 111, 16309–16313 (2014).
- T. Watashige et al., Evidence for time-reversal symmetry breaking of the superconducting state near twin-boundary interfaces in FeSe revealed by scanning tunneling spectroscopy. Phys. Rev. X 5, 031022 (2015).
- H. C. Xu et al., Highly anisotropic and twofold symmetric superconducting gap in nematically ordered FeSe_{0.93}S_{0.07}. Phys. Rev. Lett. 117, 157003 (2016).
- P. O. Sprau et al., Discovery of orbital-selective cooper pairing in FeSe. Science 357, 75-80 (2017).
- T. Hashimoto et al., Superconducting gap anisotropy sensitive to nematic domains in FeSe. Nat. Commun. 9, 282 (2018).
- D. Liu et al., Orbital origin of extremely anisotropic superconducting gap in nematic phase of FeSe superconductor. Phys. Rev. X 8, 031033 (2018).
- M. Sigrist, K. Kuboki, P. A. Lee, A. J. Millis, T. M. Rice, Influence of twin boundaries on Josephson junctions between high-temperature and conventional superconductors. *Phys. Rev. B* 53, 2925–2944 (1904).
- J. Kang, A. V. Chubukov, R. M. Fernandes, Time-reversal symmetry-breaking nematic superconductivity in FeSe. *Phys. Rev. B* 98, 064508 (2018).
- T. Hanaguri et al., Two distinct superconducting pairing states divided by the nematic end point in FeSe_{1-x}S_x. Sci. Adv. 4, eaar6419 (2018).
- A. I. Coldea et al., Evolution of the low-temperature Fermi surface of superconducting FeSe_{1-x}S_x across a nematic phase transition. npj Quant. Mater. 4, 2 (2019).

UTokyo Centre for Quantum Materials and the Canada First Research Excellence Fund, Quantum Materials and Future Technologies Program.

Author affiliations: ^aDepartment of Advanced Materials Science, University of Tokyo, Kashiwa 277-8561, Japan; ^bDepartment of Physics, Columbia University, New York, NY 10027; ^cQuantum Matter Institute, University of British Columbia, Vancouver, BC V6T 1Z4, Canada; ^dDepartment of Physics & Astronomy, University of British Columbia, Vancouver, BC V6T 1Z1, Canada; ^eCentre for Molecular and Materials Science, TRIUMF, Vancouver, BC V6T 2A3, Canada; ^fDepartment of Physics, Zhejiang University, Hangzhou 310027, China; ^gBeijing National Laboratory for Condensed Matter Physics, Beijing 100190, China; ^lInstitute of Physics, Chinese Academy of Sciences, Beijing 100190, China; ^lDepartment of Physics and Astronomy, McMaster University, Hamilton, ON L8S 4M1, Canada

Author contributions: Y.J.U. and T.S. designed research; K.M., M.Q., Q.S., Y.C., K.Y., Z.G., R.P.D., K.M.K., A.D., Y.S., M.S., T.T., Y.M., Y.G., S.G., L.F., Z.Z., F.N., G.Z., G.D., C.J., J.W.B., G.M.L., and Y.J.U. performed research; K.M., M.R., M.Q., Q.S., K.M.K., K.I., K.H., and Y.J.U. analyzed data; K.M., M.Q., Y.S., M.S., and Y.M. prepared single crystals; and T.S. wrote the paper.

The authors declare no competing interest.

This article is a PNAS Direct Submission. A.C. is a guest editor invited by the Editorial Board.

- Y. Sato et al., Abrupt change of the superconducting gap structure at the nematic critical point in FeSe_{1-x}S_x. Proc. Natl. Acad. Sci. U.S.A. 115, 1227-1231 (2018).
- Y. Mizukami et al., BCS-BEC crossover superconductivity in FeSe_{1-x}S_x: Thermodynamics of the transition. arXiv [Preprint] (2021). http://arxiv.org/abs/2105.00739 (Accessed 2 May 2023).
- D. F. Agterberg, P. M. R. Brydon, C. Timm, Bogoliubov Fermi surfaces in superconductors with broken time-reversal symmetry. *Phys. Rev. Lett.* 118, 127001 (2017).
- P. M. R. Brydon, D. F. Agterberg, H. Menke, C. Timm, Bogoliubov Fermi surfaces: General theory, magnetic order, and topology. *Phys. Rev. B* 98, 224509 (2018).
- C. Setty, S. Bhattacharyya, Y. Cao, A. Kreisel, P. J. Hirschfeld, Topological ultranodal pair states in iron-based superconductors. Nat. Commun. 11, 523 (2020).
- 22. C. Setty, Y. Cao, A. Kreisel, S. Bhattacharyya, P. J. Hirschfeld, Bogoliubov Fermi surfaces in spin- $\frac{1}{2}$ systems: Model Hamiltonians and experimental consequences. *Phys. Rev. B* **102**, 064504 (2020).
- G. M. Luke et al., Time-reversal symmetry-breaking superconductivity in Sr₂RuO₄. Nature 394, 558-561 (1998).
- 24. M. Matsumoto, M. Sigrist, Quasiparticle states near the surface and the domain wall in a $p_x \pm i p_y$ -wave superconductor. *J. Phys. Soc. Jpn.* **68**, 994-1007 (1999).
- P. K. Biśwas et al., Evidence of nodal gap structure in the basal plane of the FeSe superconductor. Phys. Rev. B 98, 180501 (2018).
- K. Matsuura et al., Maximizing T_c by tuning nematicity and magnetism in FeSe_{1-x}S_x superconductors. Nat. Commun. 8, 1143 (2017).
- Y. J. Uemura et al., Basic similarities among cuprate, bismuthate, organic, Chevrel-phase, and heavy-fermion superconductors shown by penetration-depth measurements. Phys. Rev. Lett. 66, 2665–2668 (1991).
- Y. J. Uemura, Condensation, excitation, pairing, and superfluid density in high-c superconductors: The magnetic resonance mode as a roton analogue and a possible spin-mediated pairing. J. Phys.: Condens. Matter 16, S4515 (2004).
- K. Ishida et al., Divergent nematic susceptibility near the pseudogap critical point in a cuprate superconductor. J. Phys. Soc. Jpn. 89, 064707 (2020).
- T. Hashimoto et al., Bose-Einstein condensation superconductivity induced by disappearance of the nematic state. Sci. Adv. 6, eabb9052 (2020).
- G. D. Morris, R. H. Heffner, A method of achieving accurate zero-field conditions using muonium. Physica B 326, 252–254 (2003).
- A. Suter, B. Wojek, Musrfit: A free platform-independent framework for μSR data analysis. Phys. Proc. 30, 69-73 (2012).



Supplementary Information for

Two superconducting states with broken time-reversal symmetry in $FeSe_{1-x}S_x$

Kohei Matsuura et al.

Yasutomo Uemura or Takasada Shibauchi. E-mail: yu2@columbia.edu or shibauchi@k.u-tokyo.ac.jp

This PDF file includes:

Supplementary text Figs. S1 to S3 Table S1 References for SI reference citations

Kohei Matsuura et al. 1 of 7

Supporting Information Text

 μ SR analysis.

Analysis of the magnetic fields from TRSB. Zero-field μ SR measurements were performed at the M20 beamline of TRIUMF using a He gas flow cryostat. Although the lowest temperature is about 2 K, this setup allows measurements with a very small background contribution and is suitable for the detection of often very small magnetic fields originating from TRSB. We used a mosaic sample composed of single crystals and a small amount of Apiezon-N grease. A silver plate known for its minimal muon relaxation is used to mount the mosaic sample.

In the zero-field (ZF) μ SR measurements, we assumed the time spectrum to consist of additive contributions from the target FeSe_{1-x}S_x crystals, Apiezon-N grease, and the silver plate, and adopted the fitting function of the following form

$$A_{\rm ZF}(t) = A_{\rm s}(0) \exp(-\Lambda t) + A_{\rm Ag} + A_{\rm grease} \left\{ f \exp\left[-\frac{1}{2}(\sigma_1 t)^2\right] + (1 - f) \exp\left[-\frac{1}{2}(\sigma_2 t)^2\right] \right\}.$$
 [S1]

Here, the first term (with the asymmetry $A_{\rm s}$ and the relaxation rate Λ) represents the contribution from the sample, the second term ($A_{\rm Ag}$ term) from the silver plate, and the third term ($A_{\rm grease}$ term) from the grease. Since muon relaxation in silver plates is known to be quite slow, the second term is treated as a constant without relaxation. Previously existing ZF μ SR data from Apiezon grease-only experiments at M20 and M13 in TRIUMF showed a significant relaxation as shown in Fig. S1. Therefore, it was treated as an independent term, even though the grease had only about 10 % or less of the total mosaic sample weight. As shown in Fig. S1, the grease signal exhibits no temperature dependence. We approximated the grease signal by the sum of two Gaussian relaxation components as described in Eq. (S1) and evaluate the relaxation rate. We obtained $\sigma_1 = 3.3$ [/ μ s] and $\sigma_2 = 0.694$ [/ μ s] with the ratio f = 0.256. These values for the grease were fixed in the data analysis. The function Eq. (S1) includes three volume contributions with the total asymmetry $A_{\rm total} = A_{\rm s} + A_{\rm Ag} + A_{\rm grease}$.

We also performed μ SR in transverse-field (TF) and weak transverse-field (wTF) at M20 on the same sample used in ZF measurements. The TF μ SR measurement was performed in the normal and superconducting states, with the applied field of 330 G along the c-axis. As shown by typical results in Fig. S2A-D, the time spectra change significantly as the sample undergoes a superconducting transition. In type-II superconductors, the TF precession signal exhibits relaxation due to the distribution of the internal magnetic field generated by the superconducting vortices, which leads to the shift of the peak position and the line broadening in the fast Fourier transformation profiles (Fig. S2E-H). The Ag plate contribution does not show significant relaxation. Unfortunately, TF μ SR data in grease in the same TF are not available. We did not find a significant relaxation in the overall time spectrum in the high-temperature region. In the low-temperature region, the effect of grease is expected to be minimal for the derivation of the TF relaxation rate of the superconducting sample, in view of the small volume fraction and temperature-independent nature of the grease signal. Therefore, we adopt the two-component fitting function to analyze TF data, with the first term representing contribution of the mosaic sample of the FeSe_{1-x}S_x crystals and Apiezon grease ($A_{\text{mosaic}} = A_{\text{s}} + A_{\text{grease}}$) and the second term the contribution of the silver plate;

$$A_{\rm TF}(t) = A_{\rm mosaic}(0) \exp\left(\frac{-\sigma^2 t^2}{2}\right) \cos(\gamma_\mu B_{\rm int} t + \phi) + A_{\rm Ag}(0) \cos(\gamma_\mu B_{\rm Ag} t + \phi).$$
 [S2]

In this function, $\gamma_{\mu}B_{\rm int}$, $\gamma_{\mu}B_{\rm Ag}$ are the frequencies of the precession signal under the external field, and ϕ is the initial phase shift, and σ is the relaxation rate of the muon spin inside the mosaic sample. With this function we obtain the relaxation rate from mosaic sample σ and the volume ratio of the silver plate $A_{\rm Ag}/A_{\rm total}$. For pure FeSe, our result $\sigma=0.5095$ [/ μ s] at 2K agrees well with that reported in a previous study at PSI (S1), which indicates that the effect of merging the sample and the grease contribution is insignificant. The silver plate volume ratio $A_{\rm Ag}/A_{\rm total}$ is 0.2127 for x=0, 0.431 for x=0.2, 0.343 for x=0.2. Although the experiment configurations of the TF measurements, with the incident muon spin rotated 90 degrees, is different from those of ZF and wTF without incident muon spin rotated, we approximated that the volume contribution of the silver plate is identical in the TF and ZF measurements: $A_{\rm Ag}/A_{\rm total}({\rm TF})=A_{\rm Ag}/A_{\rm total}({\rm ZF})$.

The wTF measurements were performed with the same configuration as the ZF measurements, but with an applied field of 30 G. We estimate the total asymmetry A_{total} and the baseline parameter for the ZF measurements resorting to the analysis of wTF data taken at high temperatures well above T_c by using Eq. (S2) with $A_{\text{Ag}}/A_{\text{total}}$ fixed to the value obtained from (high) TF measurements. A_{total} is 0.2231 for x=0, 0.2406 for x=0.2, 0.21083 for the x=0.22 system. With these A_{total} fixed, we perform global fitting of the ZF data through all temperature points with Eq. (S1). Here we determine the relaxation rate from the sample Λ as a free (temperature-dependent) parameter and the ratio of the sample contribution in the total asymmetry without silver plate contribution, $A_s/(A_{\text{total}}-A_{\text{Ag}})$, as a common (temperature-independent) parameter through all runs. This analysis yields the common parameter $A_s/(A_{\text{total}}-A_{\text{Ag}})$ given as 0.9612 for x=0, 0.8927 for x=0.2, and 0.873 for x=0.22. These values are reasonable because the weight of the grease is around 10 % in the mosaic sample. The temperature dependence of the relaxation rate Λ in the first term of Eq. (S1), obtained in this analysis, is shown in Fig. 2D-F of the main text.

From the temperature dependence of the relaxation rate, we derive the magnitude of the internal field from the following relation,

$$\Lambda_{\text{total}}(T) = \Lambda_s(T) + \Lambda_n.$$
 [S3]

Here, $\Lambda_{\text{total}}(T)$ is the total relaxation rate, which includes the relaxation rate due to the field originating from TRSB in the superconducting state $(\Lambda_{s}(T))$ and the relaxation rate due to dilute isotopic nuclear spins of FeSe_{1-x}S_x and possible additional

2 of 7 Kohei Matsuura et al.

isolated impurities (Λ_n) . These two static local magnetic field sources are considered to be independent and dilute, which give rise to Lorentz-type static magnetic field distributions and the observed exponential decay in the time spectra. In this case, the two contributions add up linearly as shown in Eq. (S3). This can be understood by remembering that the static relaxation rate of a dilute alloy spin glass is proportional to the concentration of magnetic elements, as shown in the previous studies by Uemura et al. (S2). From the relaxation rate $\Lambda_s(T)$, the magnetic field strength inside the superconducting sample is estimated by $B_{\rm int} = \Lambda_s(0)/\gamma_\mu$.

Analysis of superconducting penetration depth. The ZF data for TRSB are taken at the M20 beamline only, because the dilution cryostat for temperatures below $T \sim 4$ K at the M15 beamline has a significant stray magnetic fields from the superconducting magnet. As for the TF measurements of the superfluid density, we used both the M20 and M15 beamlines. These two experimental setups had different conditions with different sample volumes. The data at M15 with dilution fridge have a significant background contribution due to muons stopping in the cold-finger sample holder and surrounding materials. Moreover, we use the Cu-glue for attaching the single crystals to the silver plate. Therefore, the absolute values of the penetration depth from M15 data are less reliable compared with the data at M20. We analyze the TF data for all samples by comparing the data from the two beamlines. The data at M20 are globally fitted, with Eq. (S2) and the procedure described above. We obtained the sample relaxation rate at T=2 K at M20. Then, this result is applied as the fixed parameter for the fitting of the data at 2 K from M15 and the dataset at M15 is globally fitted with the referred parameters from the 2 K data.

The contribution of the superconducting vortices in the TF relaxation rate is calculated by quadratically subtracting the nuclear dipole relaxation rate; $\sigma_s^2 = \sigma^2 - \sigma_n^2$. This relaxation is related to the London penetration depth in the vortex state through the equation given by (S1)

$$\frac{\sigma_{\rm sc}(T)}{\gamma_{\mu}} = 0.06091 \frac{\Phi_0}{\lambda^2(T)}.$$
 [S4]

The obtained temperature dependence of the superfluid density $\lambda^{-2}(T)$ is shown in Fig. 3A. Our data for FeSe (x=0) can be compared with the previous report of TF- μ SR measurements with a 500-G c-axis field by using FeSe crystals grown by a flux method (S1) (Fig. S3). Although the measurement fields are slightly different and sample growth methods are different, the obtained superfluid density $\lambda^{-2}(T)$ data are in good agreement.

Estimate of superfluid density from the electronic structure in $\text{FeSe}_{1-x}\mathbf{S}_x$. In general, λ_i^{-2} (i=a,b,c) at absolute zero is given by

$$\lambda_i^{-2}(0) = \frac{\mu_0 e^2}{4\pi^3 \hbar} \oint_{FS} \frac{(v_F^i)^2}{|v_F|} dS_k,$$
 [S5]

where v_F^i is the *i*-axis component of the Fermi velocity v_F and the integral is taken over the Fermi surface. If one considers an isotropic 2D cylindrical Fermi surface, the in-plane $\lambda_{ab}^{-2}(0)$ can be given by

$$\lambda_{ab}^{-2}(0) = \frac{\mu_0 e^2}{4\pi^3 \hbar} \int_0^{2\pi} v_F^{ab} \cos^2 \theta k_F^{ab} k_F^c d\theta = \frac{\mu_0 e^2}{4\pi^2 \hbar} v_F^{ab} k_F^{ab} k_F^c = \frac{\mu_0 e^2}{d} \frac{n_{\rm 2D}}{m^*} = \frac{\mu_0 e^2 n_{\rm 3D}}{m^*},$$
 [S6]

where v_F^{ab} is the in-plane Fermi velocity, $k_F^{ab(c)}$ is the in-plane (out-of-plane) Fermi wavenumber, d is the c-axis length, and m^* is the in-plane effective mass (note that the two relations, $v_F^{ab} = \hbar k_F^{ab}/m^*$ and $n_{3D} = n_{2D}/d = (k_F^{ab})^2 k_F^c/(4\pi^2)$, hold). However, when the Fermi surface is anisotropic, one needs to consider the \mathbf{k} dependence of the Fermi velocity to calculate $\lambda^{-2}(0)$. For FeSe_{1-x}S_x, we evaluated the value of $\lambda^{-2}(0)$ considering the multiple Fermi surfaces observed in quantum oscillations experiments (S3), including their dimensionality. In quantum oscillations experiments, we can obtain information on the effective mass and Fermi wavenumber of extremal orbits, from which we can estimate $\lambda^{-2}(0)$. The Fermi wavenumber k_F of the extremal orbit is given by the oscillation frequency F as follows: $k_F = (2eF/\hbar)^{1/2}$ (S4).

FeSe has a multiband electronic structure with hole- and electron-like cylindrical Fermi surfaces near the zone center and corner, respectively (S5). From quantum oscillations, it has been assigned that α and γ orbits are extremal orbits on an electron Fermi surface, while β and δ orbits are from a hole Fermi surface (S3, S4). This assignment provides an estimate of the Sommerfeld constant consistent with the experimental value, implying that almost all carriers are explained by these two Fermi surfaces. In FeSe_{1-x}S_x, the electron Fermi surface (α/γ -orbits) remains quasi-two-dimensional as x increases, while the hole Fermi surface (β/δ -orbits) becomes more three dimensional with increasing x, resulting in a three-dimensional pocket (δ -orbit) for x > 0.12 (S3). We evaluated $\lambda^{-2}(0)$ of the electron Fermi surface by calculating n_{3D}/m^* for the α and γ orbits and averaging them. For the hole Fermi surface, we calculated $\lambda^{-2}(0)$ by assuming a truncated cone-shaped Fermi surface for x > 0.12 and an elliptical Fermi surface for x > 0.12. In the former case, if we regard the hole Fermi surface as two truncated cones, we find $n_{3D} = 2\frac{1}{4\pi^2}\frac{1}{3}\frac{\pi}{d}(k_{F,\beta}^2 + k_{F,\beta}k_{F,\delta} + k_{F,\delta}^2)$, while in the latter case, assuming an elliptical Fermi surface whose radius in the k_c direction is half of the Brillouin zone, we obtain $n_{3D} = \frac{1}{3\pi^2}\frac{\pi}{d}k_{F,\delta}^2$, where $k_{F,\beta(\delta)}$ is the Fermi wavenumber of the $\beta(\delta)$ orbit. Here, we used the averaged effective mass of the β and δ orbits for the hole Fermi surface. Note that for $x \gtrsim 0.07$, a three-dimensional hole pocket (χ -orbit) appears (S3), but its contribution to the total $\lambda^{-2}(0)$ is at most 5%, and thus we ignore it. For x = 0, we get $\lambda^{-2} = \lambda_{electron}^{-2} + \lambda_{electron}^{-2} = 5.15 \,\mu\text{m}^{-2}$ (see Table S1). This corresponds to $\lambda = 440 \,\text{nm}$, which is close to the previously reported values of $\lambda = 415$ (391) nm from μ SR measurements for 500 (120) G (S1) and $\lambda \approx 400 \,\text{nm}$ m

Kohei Matsuura et al. 3 of 7

Table S1. Values of $\lambda^{-2}(0)$ estimated from quantum oscillations experiments in FeSe (S3).

FS	Orbit	m^*/m_0	$F\left[\mathrm{kT}\right]$	$k_F [\mathrm{\AA}^{-1}]$	$\lambda^{-2}(0) [\mu \text{m}^{-2}]$
electron	α	1.9	0.11	0.057	2.24
	γ	6.7	0.57	0.13	
hole	β	4.3	0.20	0.078	2.90
	δ	4.6	0.66	0.14	

References

- [S1] Biswas PK, et al. (2018) Evidence of nodal gap structure in the basal plane of the FeSe superconductor. *Phys. Rev. B* 98(18):180501.
- [S2] Uemura YJ, Yamazaki T, Harshman DR, Senba M, Ansaldo EJ (1985) Muon-spin relaxation in AuFe and CuMn spin glasses. Phys. Rev. B 31(1):546-563.
- [S3] Coldea AI, et al. (2019) Evolution of the low-temperature Fermi surface of superconducting $FeSe_{1-x}S_x$ across a nematic phase transition. $npj\ Quant.\ Mater.\ 4(1):2.$
- [S4] Terashima T, et al. (2014) Anomalous Fermi surface in FeSe seen by Shubnikov-de Haas oscillation measurements. *Phys. Rev. B* 90(14):144517.
- [S5] Shibauchi T, Hanaguri T, Matsuda Y (2020) Exotic superconducting states in fese-based materials. J. Phys. Soc. Jpn. 89(10):102002.
- [S6] Kasahara S, et al. (2014) Field-induced superconducting phase of FeSe in the BCS-BEC cross-over. *Proc. Natl. Acad. Sci. USA* 111(46):16309–16313.
- [S7] Hashimoto K, et al. (2010) Evidence for superconducting gap nodes in the zone-centered hole bands of KFe₂As₂ from magnetic penetration-depth measurements. *Phys. Rev. B* 82(1):014526.
- [S8] Fletcher JD, et al. (2009) Evidence for a nodal-line superconducting state in LaFePO. Phys. Rev. Lett. 102(14):147001.

4 of 7 Kohei Matsuura et al.

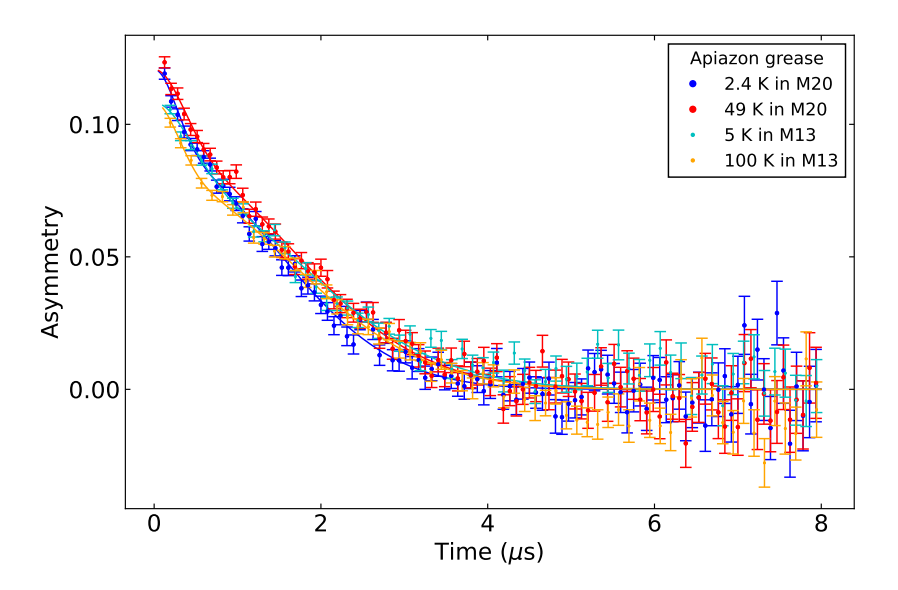


Fig. S1. Time spectra of the Apiezon grease as a reference for a background contribution. In this study, the collection of $FeSe_{1-x}S_x$ samples are placed on the silver plate with the Apiezon grease. To evaluate the grease contribution, the data for the previous grease-only experiments taken at M20 and M13 beamlines (dots) were analyzed by the relaxation with two Gaussian components (curves). The data in two beamlines consistently show temperature-independent relaxations.

Kohei Matsuura et al. 5 of 7

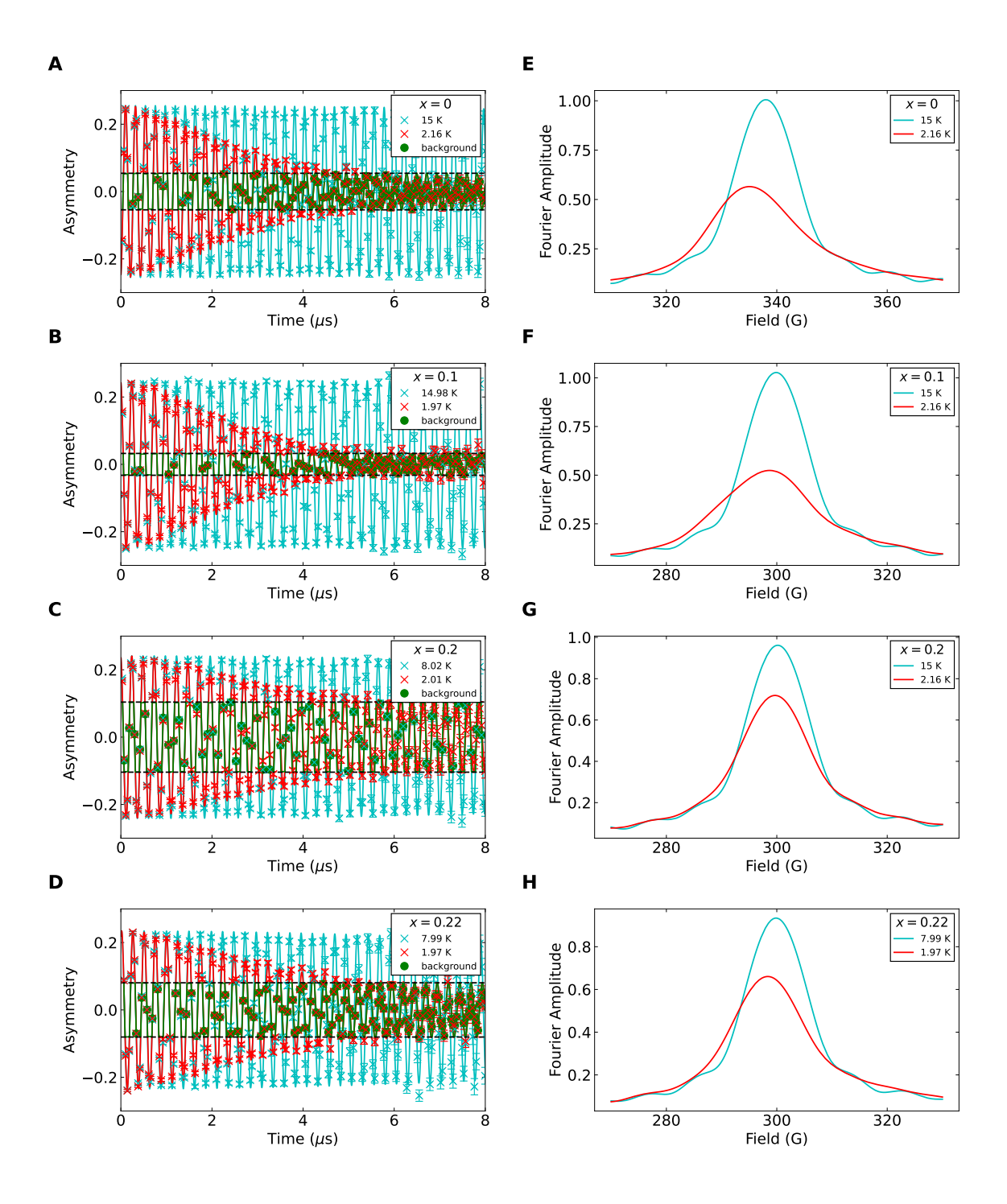


Fig. S2. Transverse-field μ SR spectra. (A-D) μ SR time spectra above (light blue) and below T_c (red) in FeSe $_{1-x}$ S $_x$ for x=0 (A), 0.10 (B), 0.20 (C), and 0.22 (D). There is an offset in the relaxation (green part), which comes from the contributions of muons decaying from the silver plate and grease. From this, we can determine the background contribution. (E-H) Fast Fourier transformations of the spectra above (light blue) and below T_c (red). Below T_c , the peak position is shifted and the line shape is broadened, reflecting the field distributions in the vortex state.

6 of 7 Kohei Matsuura et al.

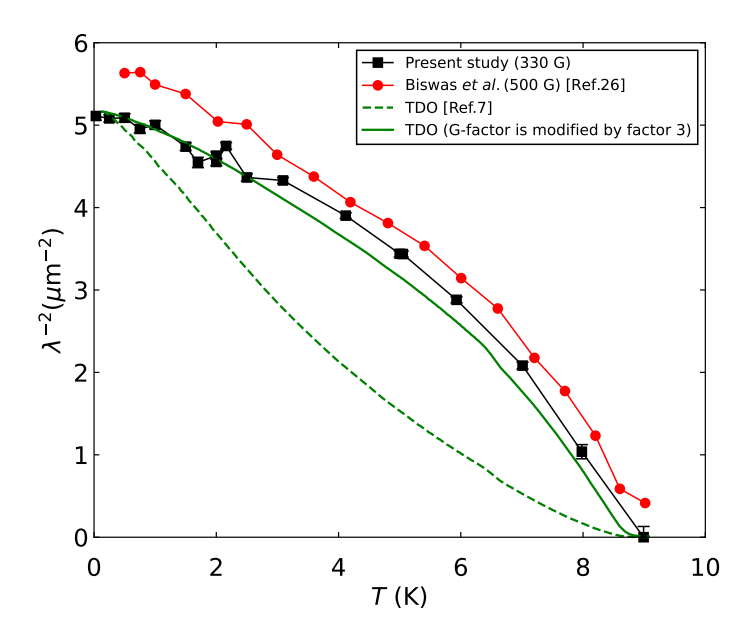


Fig. S3. Comparison of the superfluid density in FeSe with the previous measurements. Temperature dependence of the superfluid density $\lambda^{-2}(T)$ in our 330-G TF- μ SR measurements for FeSe (black squares) is compared with the reported 500-G TF- μ SR measurements (red circles) (S1) and the tunnel diode oscillator (TDO) measurements (green dashed line) (S6). For the TDO data, it has been pointed out for the iron-based superconductors that surface roughness of the cut edges can lead to errors in the geometrical factor G, which affect the overall curvature of $\lambda^{-2}(T)$ (S7, S8). When we modify the G value by a factor of 3 and use $\lambda(0)=440$ nm for the TDO data (green solid line), we obtain $\lambda^{-2}(T)$ consistent with our TF- μ SR data.

Kohei Matsuura et al. 7 of 7

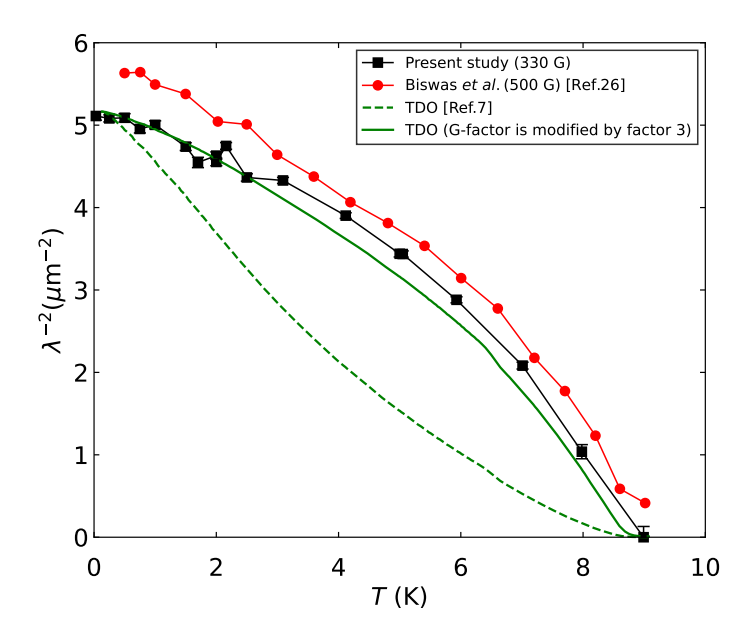


Fig. S3. Comparison of the superfluid density in FeSe with the previous measurements. Temperature dependence of the superfluid density $\lambda^{-2}(T)$ in our 330-G TF- μ SR measurements for FeSe (black squares) is compared with the reported 500-G TF- μ SR measurements (red circles) (S1) and the tunnel diode oscillator (TDO) measurements (green dashed line) (S6). For the TDO data, it has been pointed out for the iron-based superconductors that surface roughness of the cut edges can lead to errors in the geometrical factor G, which affect the overall curvature of $\lambda^{-2}(T)$ (S7, S8). When we modify the G value by a factor of 3 and use $\lambda(0)=440$ nm for the TDO data (green solid line), we obtain $\lambda^{-2}(T)$ consistent with our TF- μ SR data.

Kohei Matsuura et al. 7 of 7